





Origin of the Shell Structure in the Primary Outflow from IRAS 15398-3359

TOMOYUKI HANAWA ¹, YUKI OKODA ^{2,3}, YAO-LUN YANG ³, AND NAMI SAKAI ³

¹Center for Frontier Science, Chiba University, 1-33 Yayoi-cho, Inage-ku, Chiba 263-8522, Japan

²NRC Herzberg Astronomy and Astrophysics, 5071 West Saanich Road, Victoria, BC, V9E 2E7, Canada

³Star and Planet Formation Laboratory, RIKEN Cluster for Pioneering Research, Wako-shi, Saitama, 351-0106, Japan

(Received March 31, 2025; Revised May 8, 2025; Accepted May 12, 2025)

Submitted to The Astrophysical Journal

ABSTRACT

IRAS 15398-3359, a Class 0 protostar in Lupus I star forming region, is associated with three generations of outflows. The primary outflow, i.e., the most recent one, shows internal structure named “shell structure” in the near infrared emission map. The shell structure is also seen in the emission lines of CO, H₂CO, and others species. We find a similar structure in an underexpanded jet produced in aerodynamics and other engineering applications. A high pressure gas ejected through a nozzle expands to form a supersonic flow. When the pressure of the ejected gas becomes lower than that of the ambient gas, the jet is compressed to form a shock wave. The shock heated gas expands again to form substructures along the jet. We examine the similarity between the primary outflow of IRAS 15398-3359 and industrial underexpanded jet and the possibility that the shell structure of the former is due to repeated expansion and compression in the direction perpendicular to the jet propagation.

Keywords: Star formation (1569); Protostars (1302); Stellar jets (1607)

1. INTRODUCTION

Jets and outflows are important signatures of protostars. They emerge within 100 au from a protostar and can reach a few parsec away from the origin. Recent high resolution imaging observations with ALMA and JWST are valuable for studying their launch. IRAS 15398–3359 is one of the sources that both ALMA and JWST have observed to obtain sub-arcsecond images in the radio and infrared wavelengths.

IRAS 15398–3359 is a Class 0 protostar in the Lupus I star forming region located at a distance of $154.9^{+3.2}_{-3.4}$ pc (Galli et al. 2020) and is associated with multiple outflows. Tachihara et al. (1996) discovered a CO outflow with a 4m single dish telescope. Oya et al. (2014) observed the primary outflow extended in the northeast and southwest with ALMA. The northeastern and southwestern outflows are red- and blue-shifted respectively. Okoda et al. (2021a) discovered a secondary outflow extending to the southeast. The secondary out-

flow is 8'' away from the protostar on the plane of the sky, while the primary outflow seems to be connected to the protostar. Sai et al. (2024) discovered another pair of outflows at a distance of 30'' – 75'' in the northern and southern regions. This third outflow is also reported by Guzmán Ccolque et al. (2024). The secondary and third outflows indicate that the outflow activity of IRAS 15398–3359 is episodic and the primary outflow is due to the most recent activity (Okoda et al. 2021a; Sai et al. 2024; Guzmán Ccolque et al. 2024). Since these three generations of outflow extend in different directions, they are likely to be driven by different alignment channels.

The primary outflow has an internal structure. The integrated intensity of H₂CO (3_{0,3} – 2_{0,2}) emission line shows a node at a distance of $\sim 5''$ in the blue-shifted outflow (see Figure 1(a) of Okoda et al. 2021a). Vazzano et al. (2021) shows the change in the intensity-weighted line-of-sight velocity in ¹²CO ($J = 2 - 1$) near this node. The infrared image taken with JWST shows four shells also in the blue-shifted outflow (Yang et al. 2022). Figure 1, the reproduction of Figure 1 of Okoda et al.

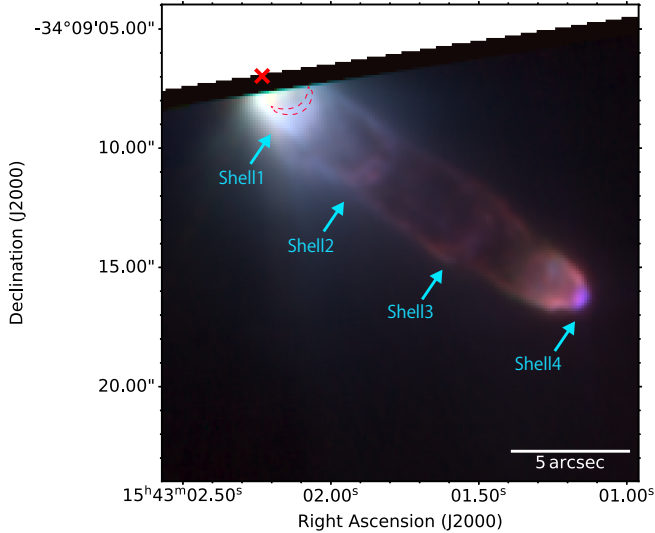


Figure 1. RGB image built from a composite of the three filter (F560W, F770W, and F1000W) MIRI images. The angular separation $5''$ correspond to the deprojected distance of 824 au for the assumed inclination angle of 20° (Oya et al. 2014). Reproduction of the top panel of Figure 1 of Okoda et al. (2025).

(2025), shows the infrared emission obtained with the three filters (F560W, F770W, and F1000W) of JWST by a composite image. The base of the primary outflow is bright in infrared. Since the infrared emission is rich in the rotational transition of H_2 molecules (Yang et al. 2022), the outflow gas is hot ($T \gtrsim 10^3$ K) at least within the regions of several hundreds au (see Okoda et al. 2025, for the temperature distribution). The thermal energy may accelerate the outflowing gas. Since the internal structure seen in the infrared emission is correlated with that observed in the radio line emissions, they are likely to have a common origin.

A possible origin of the internal structure is time variability of the outflow activity. Vazzano et al. (2021) considered a scenario that IRAS 15398–3359 has undergone four accretion outbursts which have initiated four times of outflow activities. Another possibility is magnetohydrodynamical instability of the outflow (see, e.g., Shang et al. 2023). However, these scenarios are not conclusive. It is worth seeking another possibility as an origin of the internal structure in the primary outflow.

Jets and outflows have been studied for more than a half century in aeronautical engineering (see, e.g., Franquet et al. 2015, for a review). A high pressure gas emerging from a nozzle evolves into a supersonic flow called “underexpanded outflow.” Figure 2 shows the internal structure of the underexpanded outflow for a high jet/ambient over pressure ratio schematically. For simplicity, we omitted expansion fans often included in

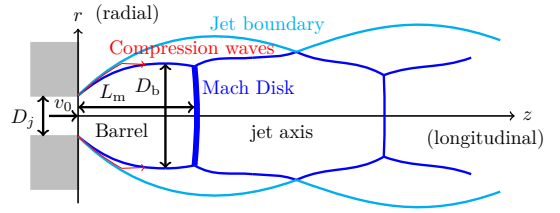


Figure 2. A schematic view of an underexpanded outflow from a nozzle. The blue curves denote the shock waves and highlighted by the thick curve is the Mach disk. The cyan curves denote the jet boundary, i.e., the boundary between the outflowing and ambient gases. The symbols and letters explain the terminology used in the text.

the similar diagrams. The initially high pressure gas expands preferentially in the direction normal to the exit plane of the nozzle to be collimated. It is well known that the underexpanded jet outflow has “barrel structure”, i.e., semi-periodic change in the outflow width. The barrel closest to the nozzle is bounded by shock waves (see Figure 2). The thick blue line is called Mach disk where the gas is highly compressed through a shock. The side of the barrel is bounded by oblique shocks. The jet gas is decelerated once to be hot, dense, and subsonic at the shock. The gas decelerated at the Mach disk expands again to be accelerated and repeats expansion from and convergence to the jet axis. We think that a similar mechanism is responsible for the shell structure of IRAS 15398–3359.

In this paper we compare IRAS 15398–3359 and engineering underexpanded jet outflow and its substructure to examine the possibility that the former’s shell structure and latter’s barrel structure are formed by the same physical mechanism. If they have a common origin, we can repurpose the knowledge in industrial science for our understanding of protostellar outflows.

This paper is organized as follows. We analyze the outflow from IRAS 15398–3359 using the archival data of ALMA and JWST in §2. We review the underexpanded jet outflow in §3 and show a simple hydrodynamic model in §4. Discussions and conclusion are given in §5.

2. OBSERVATIONS

2.1. Observation Specifications

Our analysis is based on the archival data of ALMA and JWST. The H_2CO ($3_{0,3} - 2_{0,2}$) and CS ($J = 5 - 4$) lines were observed in the project 2018.1.01205.L (PI: Satoshi Yamamoto), as a part of ALMA large program FAUST (Codella et al. 2021, <http://faust-alma.riken.jp>). The ^{12}CO ($J = 2 - 1$) line was taken from the ALMA archival data (2013.1.00879.S; Yen et al.

2013). The observation parameters are described by Okoda et al. (2021a), Okoda et al. (2023), and Yen et al. (2017). The data reduction details of both data are also given by Okoda et al. (2025).

The MIRI images and spectral cubes were taken with the Medium Resolution Spectroscopy (MRS) by the JWST CORINOS program (Yang et al. 2022) (program 2151, PI: Y.-L. Yang). The imaging data were reduced with JWST calibration pipeline v.1.14.0 (Bushouse et al. 2024) using the calibration reference data `jwst_1231.pmap`, while the spectroscopic data were reduced with JWST calibration pipeline v.1.12.5 (Bushouse et al. 2023) using the calibration reference data `jwst_1183.pmap`. The MIRI images were taken with three filters, F560W, F770W, and F1000W, centered at 5.6, 7.7, and 10.0 μm , respectively. The FWHM of the PSF ranges from $0''.207$ to $0''.328$. We use the imaging data taken simultaneously with the spectroscopic observation pointing toward a dedicated background position, because the field of view (FoV) of the image serendipitously covers the blue-shifted outflow of IRAS 15398–3359. The MRS data cover the 4.9–28 μm range with four integral field units, which have their FoVs range from $3''.2 \times 3''.7$ to $6.6'' \times 7.7''$. The spectral resolving power ($\lambda/\Delta\lambda$) decreases from ~ 3700 to ~ 1300 with wavelengths.

2.2. Observation Results

Figure 1 shows the southwest part of the primary outflow by RGB image built from a composite of three filter (F560W, F770W, and F1000W) MIRI images (Okoda et al. 2025). The MIRI image shows four bright shells named shells 1, 2, 3, and 4 in the ascending distance from the protostar. As mentioned earlier, the MIRI image traces a hot molecular gas since the line emission of H_2 molecule is dominant in the filters (see, e.g., Yang et al. 2022). The shell structure implies the spatial variation in the temperature and density. The first shell is $d_{s1} = 340$ au ($2''.06$ from the protostar on the sky) while the diameter of the barrel is $D_{w1} = 322$ au ($2''.08$). The aspect ratio, $d_{s1}/D_{w1} = 1.05$, gives a clue to estimate the pressure ratio when an underexpanded outflow model is applied. The second shell is $d_{s2} = 1060$ au ($6''.42$) away from the protostar and the jet diameter is $d_{w2} = 448$ au ($2''.87$). Here, d_{s1} and d_{s2} denote the deprojected distances while D_{w1} and D_{w2} denote the projected distance on the sky. The aspect ratios derived from these numbers are also useful for assessing our model.

A similar structure is also seen in the molecular emission lines of H_2CO ($3_{0,3} - 2_{0,2}$), CS ($J = 5 - 4$) (Okoda et al. 2021b), and ^{12}CO ($J = 2 - 1$) (Vazzano et al. 2021). Not only the integrated intensity but also the

Doppler shift of molecular line emission shows features correlated with the shell structure (see Figure 4 of Vazzano et al. 2021). Throughout this paper we adopt the systemic velocity of $v_{\text{sys}} = 5.24 \text{ km s}^{-1}$, the central value measured by Yen et al. (2017) from the C^{18}O ($J = 2 - 1$) emission line. Figure 3 shows the weighted velocity distribution and position-velocity of (a) H_2CO ($3_{0,3} - 2_{0,2}$), (b) CS ($J = 5 - 4$), and (c) ^{12}CO ($J = 2 - 1$) emission lines. The left panels show the whole primary outflows while the right panels are enlargement around the protostar. The position of the protostar is designated by the plus signs on each panel. The locations of shells 1, 2, 3, and 4 are shown in the left panel of Figure 3b. Shell 1 is denoted also by the red dashed curves in the right panels. We find a semi-periodic change in the velocity not only in the blue lobe but also in the red lobe. See also Figure 4 of Thieme et al. (2023) for a higher angular resolution map of ^{12}CO ($J = 2 - 1$) around the protostar. The weighted velocity of H_2CO ($3_{0,3} - 2_{0,2}$) and CS ($J = 5 - 4$) are similar while that of ^{12}CO ($J = 2 - 1$) is slightly different. We think that the difference is mainly due to the optical depth, i.e., the abundance and excitation condition. The velocities of H_2CO ($3_{0,3} - 2_{0,2}$) and CS ($J = 5 - 4$) show only small deviation from the systemic velocity ($v_{\text{sys}} = 5.24 \text{ km s}^{-1}$) around the protostar. The line emission is clearly blue-shifted between shells 1 and 2. This velocity change implies acceleration of the outflow. The weighted velocity between shells 1 and is low especially in the CS ($J = 5 - 4$) emission. Note the red-shifted emission in the blue lobe and the blue-shifted one in the red lobe (see also Figure 2 of Okoda et al. 2025). These apparently reverse flows appear near the outflow axis. The slow and reverse flows imply deceleration. We do not find significant asymmetry with respect to the outflow axis, which means that rotation around the outflow axis is insignificant. If the outflow rotates fast, we will find a velocity gradient perpendicular to the outflow axis (see, e.g., Matsushita et al. 2021, for an example of rotating outflows). ^{12}CO ($J = 2 - 1$) shows a larger and smoother deviation from the systemic velocity (note that the color scale of ^{12}CO ($J = 2 - 1$) is different from those of H_2CO ($3_{0,3} - 2_{0,2}$) and CS ($J = 5 - 4$)). Still we find a similar decrease in the weighted velocity between shells 2 and 3 in ^{12}CO ($J = 2 - 1$). All the lines show the northwestern hole of a slow (or reverse) flow at a distance of $\sim 7''$ (~ 1000 au) from the protostar.

Figure 4 shows the position velocity diagrams for H_2CO ($3_{0,3} - 2_{0,2}$) and CS ($J = 5 - 4$) along the outflow axis shown in the left panel of Figure 3a. The vertical dotted lines denote the locations of shells 1, 2, and 3. They show a red component in addition to a blue com-

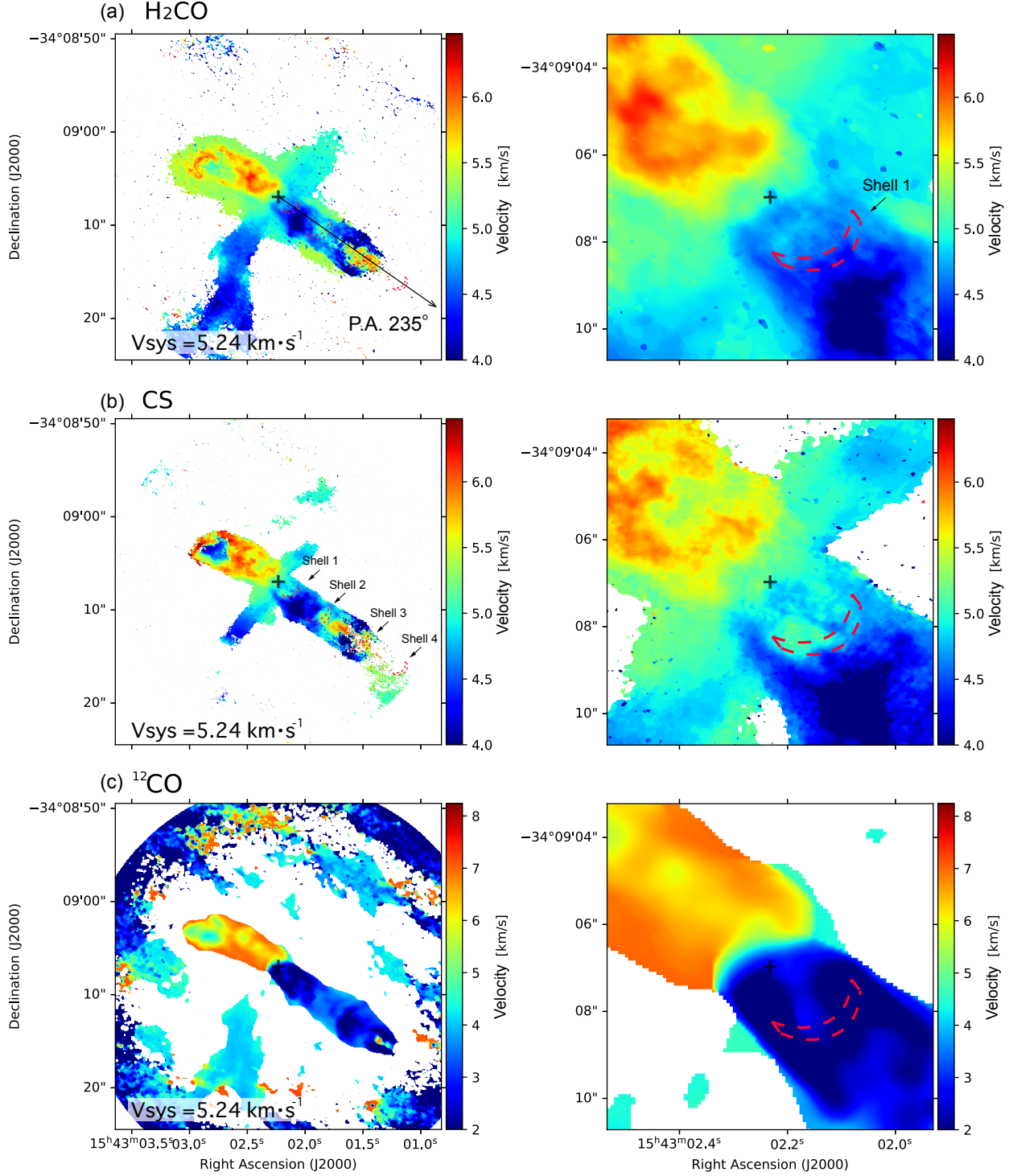


Figure 3. Moment 1 maps of (a) H_2CO ($3_{0,3} - 2_{0,2}$) (b) CS ($J = 5 - 4$) and (c) ^{12}CO ($J = 2 - 1$). The right panels are the enlargement of the left panels around the protostar (+). The jet axis (P.A. 235°) and the shell locations are shown in the left panels of (a) and (b), respectively. The red dashed curves in the right panels represent shell 1 shown in Fig. 1.

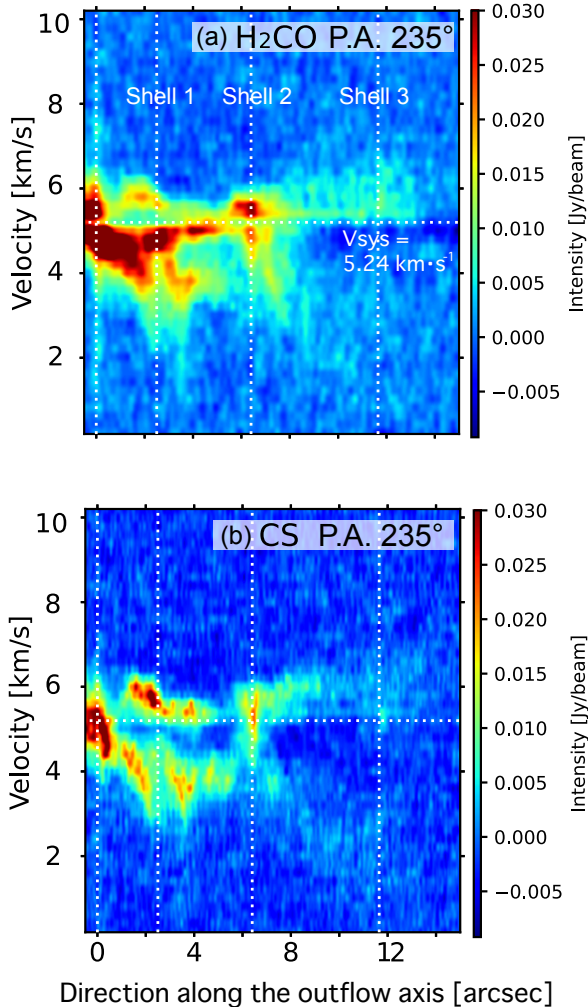


Figure 4. PV diagrams along the outflow axis (P.A. 235°). The white dotted lines show the positions of the four shell structures. The systemic velocity of 5.24 km s^{-1} is shown in the horizontal dotted lines.

ponent in the interval between the protostar and shell 3. The blue component shows a steep velocity gradient suggesting acceleration and terminates at shell 1. The red component appears around $1''$ ($\sim 150 \text{ au}$) from the protostar. The red component of CS ($J = 5 - 4$) looks to continue beyond shell 2 while changing the velocity and intensity. We find another steep velocity gradient starting from shell 1. Existence of the two components imply either diverging or converging flow along the line of sight, i.e., in the direction perpendicular to the outflow axis. The velocity gradient is more likely to be due to acceleration/deceleration in the outflow rather than the initial velocity at the time of ejection.

Okoda et al. (2025) derived the temperature and column density of H_2 molecules from the JWST MIRI MRS observations, which covers a $\sim 3'' - 5''$ region around

the protostar (see their Figures 4a and 4b for the temperature and column density, respectively). The temperature is as high as $\sim 1300 \text{ K}$ near the protostar and decreases with the distance below 1000 K at shell 1. The column density is as high as $N \simeq 10^{20} \text{ cm}^{-2}$ around the protostar and decreases to $N \simeq 10^{19.5} \text{ cm}^{-2}$ near shell 1.

Infrared emission from ionized elements supports the idea that the outflow gas is hot. Figure 5 show continuum-subtracted intensity of $[\text{Fe II}]$ $25.99 \mu\text{m}$, $17.935 \mu\text{m}$, and $[\text{Ne II}]$ $12.81 \mu\text{m}$. The blue background denotes MIRI F560W image taken with JWST (Yang et al. 2022). $[\text{Fe II}]$, $[\text{Ne II}]$, and $[\text{Ne II}]$ emissions are strong around the protostar and between the first and second shells. In other words, they have a gap near the first shell, which is consistent with the temperature derived from H_2 line emissions. These ionized elements also show the substructure correlated with the shell structure. Differences among the line emissions maps are mostly due to the wavelength dependent angular resolutions.

The temperature decrease with the distance from the protostar is not likely to be radiative cooling. If the thermal energy is lost by radiative cooling, we need another heating source for the hot region between shells 1 and 2. It is likely to be due to adiabatic expansion, which is consistent with the decrease in the column density and the increase in the blue-ward shift in the emission line. The adiabatic expansion converts thermal energy into a kinetic one, which can be used to heat up again the gas through a shock wave.

3. UNDEREXPANDED JET

A high pressure gas emerging from a nozzle evolves into an underexpanded jet. The study of such a jet has a long history. It can be traced back to the 19th century. A review by Franquet et al. (2015) summarizes the history and current knowledge. Though many numerical simulations have been done for astronomical jets and outflows, most of them are focused on the launch and collimation. Some simulations are focused on the internal structure, i.e., the formation of the Mach disk (see, e.g., Norman et al. 1982; Komissarov & Falle 1998; Smith & Keogh 2022; Smith & Richards 2023) and related structure. However, industrial jets have been studied much more intensively and the theory is verified by experiments and well established. Thus, we refer to Franquet et al. (2015) in the following since other reviews show essentially the same results.

In aeronautical science, the jet is divided into three zones: (1) the nearfield zone, (2) the transition zone, and (3) the farfield zone (see, e.g., Franquet et al. 2015).

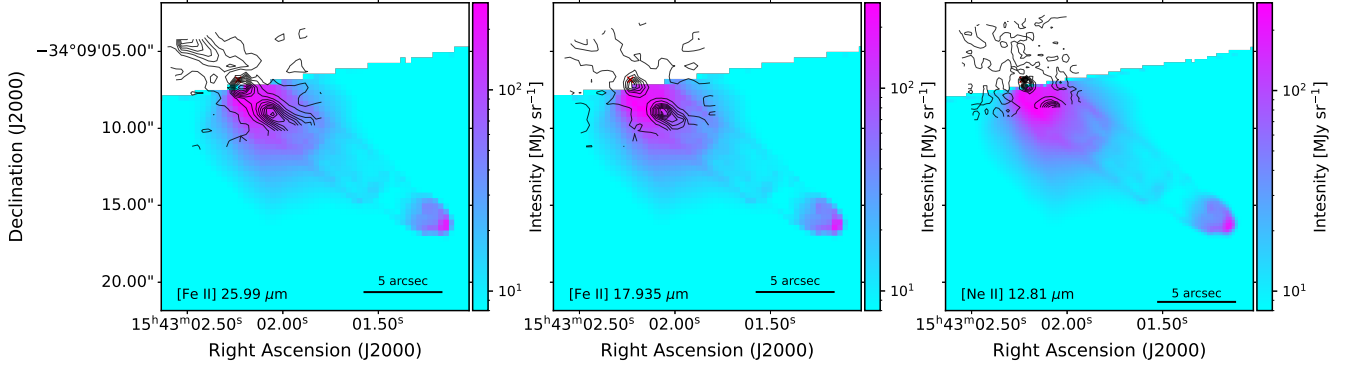


Figure 5. Contours show intensities of (left) [Fe II] 25.99 μm , (center) 17.935 μm , and (right) [Ne II] 12.81 μm taken with JWST (Yang et al. 2022). The color denotes MIRI image taken with F560W filter on JWST.

The nearfield zone is further divided into two components: the core and the mixing layer. The gas expands adiabatically in the core, where the pressure, density, and temperature decreases with distance from the end of nozzle. The pressure gradient accelerates the ejected gas to be supersonic. The supersonic jet undergoes a shock and gets compressed to be hot and dense. The structure made by the shock is called the Mach disk. The jet between the nozzle end to the Mach disk is named “barrel” from its appearance (see Figure 2). The jet width is controlled by the pressure balance between the jet and the ambient gas. The hot dense gas ahead of the Mach disk is accelerated again to form subsequent substructures along the jet axis.

The morphology and structure of the jet depends mainly on the pressure ratio, P_0/P_∞ , where P_0 and P_∞ denote the initial pressure of the injected gas and the ambient gas pressure, respectively. The distance to the Mach disk (L_m) is proportional to the diameter of the nozzle (D_j). Crist et al. (1966) derived an approximate formula,

$$\frac{L_m}{D_j} = \sqrt{\frac{P_0}{2.4 P_\infty}}, \quad (1)$$

analytically. Young (1975) discussed that the coefficient in Equation (1) should be a function of the specific heat ratio, though the dependence is weak. Equation (1) is valid for a wide range of P_0/P_∞ . Hatanaka & Saito (2012) examined the effects of the nozzle shape on the aspect ratio. Equation (1) gives a fairly good fit in the range $14 \lesssim P_0/P_\infty \lesssim 80$ when the nozzle is either straight or divergent. Equation (1) overestimate D_m/D_j a little when the nozzle is straight. We can expect Equation (1) gives a good estimate for an astronomical jet though it does not emerge from a nozzle.

The pressure ratio controls the ratio between the diameters of the Mach disk and jet nozzle. Addy (1981)

derived an empirical formula

$$\frac{D_m}{D_j} = 0.36 \sqrt{\frac{P_0}{P_\infty}} - 3.9, \quad (2)$$

for smooth convergent nozzle, where D_m denotes the diameter of the Mach disk. The ratio depends only slightly on the nozzle shape in particular when the pressure ratio is high.

When the pressure ratio is high, the jet is variable. Though the flow in the core is laminar, the flow beyond the Mach disk is turbulent. See Figure 3 of Yu et al. (2013) shows the instantaneous and time-averaged images of the jet for $P_0/P_\infty = 10$.

We can evaluate the acceleration of the jet gas applying the Bernoulli’s theorem. When the flow is stationary adiabatic in the barrel, the sum of the kinetic energy and specific enthalpy

$$H = \frac{1}{2}v^2 + \frac{\gamma P}{(\gamma - 1)\rho} = \frac{1}{2}v_0^2 + \frac{\gamma P_0}{(\gamma - 1)\rho_0}, \quad (3)$$

is constant along the stream line, where v , ρ , and γ denote the velocity, density, and specific heat ratio, respectively. Given the initial velocity is much lower than the sound speed ($|v_0| \ll \sqrt{\gamma P_0/\rho_0}$), the jet becomes transonic when the temperature reaches $T = 2T_0/(\gamma + 1)$. The specific enthalpy is evaluated to be

$$\frac{\gamma P}{(\gamma - 1)\rho} = (5.0 \text{ km s}^{-1})^2 \left(\frac{T}{2000 \text{ K}} \right), \quad (4)$$

for a molecular gas having the mean molecular weight, $\mu = 2.3 m_H$. Equation (4) provides an estimate for the gas velocity accelerated by the pressure.

4. HYDRODYNAMIC MODEL

4.1. Model Setting

We make a hydrodynamic model to reproduce the shell structure seen in IRAS 15398–3359. For simplicity

we assume that the outflow source maintain high temperature and high density. We ignore gravity, magnetic field, radiative cooling/heating processes for simplicity.

We use the cylindrical coordinates, (r, φ, z) and assume the symmetry in the φ -direction ($\partial/\partial\varphi = 0$). Thus, the density (ρ), pressure (P), and velocity ($\mathbf{v} = (v_r, v_z)$) are functions of (r, z, t) , where t denotes the time, which is set to be $t = 0$ at the initial stage, i.e., the onset of the outflow ejection. The gas is assumed to be an ideal gas having the mean molecular weight $\mu = 2.3$ and the specific heat ratio, $\gamma = 7/5$. Then the pressure and density are expressed as

$$P = nk_{\text{B}}T, \quad (5)$$

$$\rho = \mu m_{\text{H}}n, \quad (6)$$

where k_{B} and m_{H} denote the Boltzmann constant and the mass of hydrogen atom, respectively. We use the number density (n) and temperature (T) instead of P and ρ when we show our numerical results.

We assume a geometrically thin gas disk placed at $z = 0$ and consider the half space above the disk plane ($z > 0$). The half space is occupied initially by an ambient gas of which density and pressure are ρ_{∞} and P_{∞} , respectively. The ambient gas is at rest at the initial stage ($t = 0$).

We use the finite volume method in our numerical simulations. The spatial resolution, i.e., the numerical cell width is uniform at Δr in the main part of the computation domain, $0 \leq r \leq N_r \Delta r$ and $0 \leq z \leq N_z \Delta z$, where N_r and N_z are 780 and 7560, respectively. The cell width increases exponentially beyond $r > N_r \Delta r$ and $z > N_z \Delta r$. The cell width is larger by a factor of 1.25 compared to that of the inner adjacent cell. We placed 40 cells in the r - and z -directions outside the main part. Thus the outer boundary is located very far from the main part. We placed a fixed outer boundary at $r = 2.47 \times 10^4$ au and $z = 2.47 \times 10^4$ au but no disturbance reaches the outer boundary.

We set an outflow engine as a boundary condition on $z = 0$ plane. The nozzle of the jet is assumed to be a circle having the radius, R_0 . The pressure is fixed to be

$$P(r, z = 0) = \begin{cases} P_0 & (r \leq R_0 - 3\Delta r) \\ P_{\infty} & (z \geq 0) \end{cases}. \quad (7)$$

The pressure decreases from P_0 to P_{∞} in the $R_0 - 3\Delta r < r < R_0$ at a constant rate. The density and velocity are

fixed to be

$$\rho(r, z < 0) = \begin{cases} \rho_0 & (r \leq R) \\ \rho_{\infty} & (r > R) \end{cases}, \quad (8)$$

$$v_r(r, z < 0) = 0 \quad (9)$$

$$v_z(r, z < 0) = \begin{cases} v_{\text{jet}} & (r \leq R) \\ 0 & (r > R) \end{cases}, \quad (10)$$

As summarized in Table 1 we set the initial flow to be subsonic ($v_{\text{jet}}/\sqrt{\gamma P_0/\rho_0} = 0.27$). Remember that the supersonic collimated outflow was given as the initial condition in the simulations of Norman et al. (1982), Smith & Keogh (2022), and others. Our simulations include initial acceleration and collimation though we assume hot dense gas and disk as a source of acceleration and collimation, respectively.

We use the number density, $n_0 = \rho_0/(\mu m_{\text{H}})$ and $n_{\infty} = \rho_{\infty}/(\mu m_{\text{H}})$, instead of ρ_0 and ρ_{∞} to specify the initial density distribution. We also use $T_0 = P_0/(k_{\text{B}}n_0)$ and $T_{\infty} = P_{\infty}/(k_{\text{B}}n_{\infty})$ to define the pressure distribution. We solve the hydrodynamical equations numerically with the second order accurate scheme which can capture a shock wave without spurious oscillations. We employ a flux split method based on approximate Riemann solution to avoid negative density and pressure. Our numerical code has been proved to reproduce a strong shock wave by solving the shock tube problem. It has been applied to gas accretion to a gas disk rotating around a protostar (Hanawa & Matsumoto 2021; Hanawa et al. 2022, 2024).

4.2. Canonical Model

First we show model A in which the model parameters are taken to be $n_0 = 10^7 \text{ cm}^{-3}$, $n_{\infty} = 5 \times 10^6 \text{ cm}^{-3}$, $T_0 = 2000 \text{ K}$, and $T_{\infty} = 100 \text{ K}$. Then the pressure ratio is set to be $P_0/P_{\infty} = n_0 T_0/(n_{\infty} T_{\infty}) = 40$. The jet is assumed to emerge from the circle of $R = 50 \text{ au}$ with the initial velocity $v_{\text{jet}} = 0.845 \text{ km s}^{-1}$, which is much smaller than the sound speed at 2000 K, 3.18 km s^{-1} . The spatial resolution is $\Delta r = 0.714 \text{ au}$ in the main part of the computation box of $0 \leq r \leq 557 \text{ au}$ and $0 \leq z \leq 5400 \text{ au}$. The jet emerging circle is resolved with $R/\Delta r = 70$ numerical cells.

Figure 6 shows model A by a snap shot at $t = 7.47 \times 10^3 \text{ yr}$. The top and second panels show the density (n) and the temperature (T) in the logarithmic scale by color. The third and fourth panels show the velocity (v_r, v_z). Each panel shows also the area of $r < 0$, which is flipped over from that of $r > 0$, for comparison with IRAS 15398–3359. All the panels show the Mach disk at $z \simeq 300 \text{ au}$. Though the flow is laminar in the barrel ($z \lesssim 300 \text{ au}$), it is turbulent in the

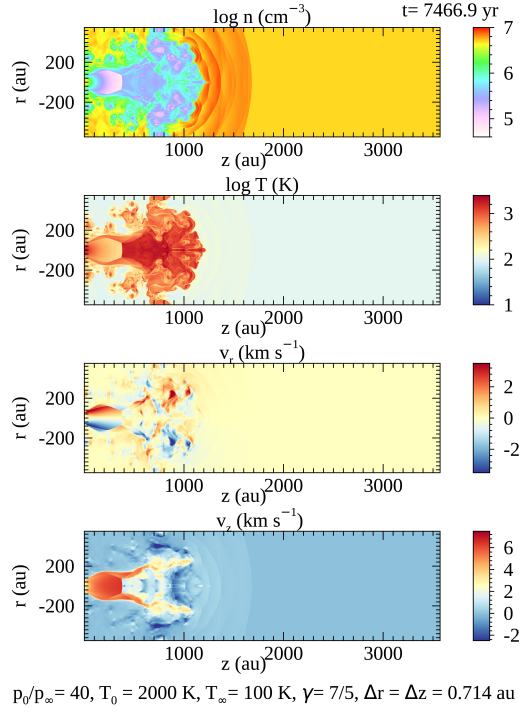


Figure 6. Each panel shows the number density (n), temperature (T), and velocity (v_r, v_z) at $t = 7.47 \times 10^3 \text{ yr}$ in model 40. The time evolution of model A is shown in the associated movie. The animation shows that the gas emerges from the left and the head proceeds rightward. The outflow is turbulent and associated with shock waves. The animation shows the sequence from zero to 443.98 years. The duration of the animation is 18 seconds.

region beyond the Mach disk. The flow is variable as shown in the animation associated with Figure 6. Still we find a semi-periodic change in the velocity, (v_r, v_z). This change is due to the pressure balance between the outflow and ambient gases. The longitudinal velocity is negative ($v_z < 0$) near $z = 1000 \text{ au}$. This substructure evolves into the second shell. The outflow compresses the ambient gas ahead of it through a shock. The shock compressed gas has the highest density and a moderate temperature of several hundreds K.

model	P_0/P_∞	n_0/n_∞	T_0	T_∞	v_{jet}
A	40	2.0	2000 K	100 K	0.85 km s^{-1}
B	62.5	3.125	2000 K	100 K	0.85 km s^{-1}
C	40	0.4	2000 K	20 K	0.85 km s^{-1}

Table 1. Model Parameters.

Figure 7 is the same as Figure 6 but shows a later stage at $t = 1.498 \times 10^4 \text{ yr}$. The outflow head reaches $z \sim 2200 \text{ au}$ and the density is highest in the shock

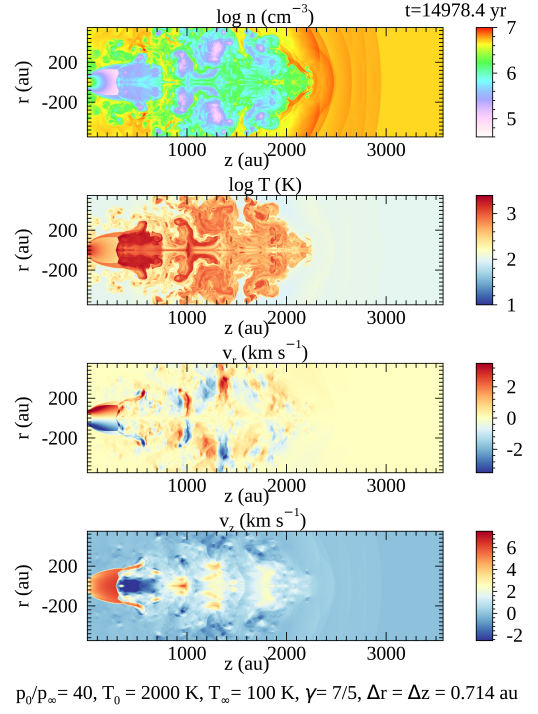


Figure 7. The same as Figure 6 but for the stage at $t = 1.498 \times 10^4 \text{ yr}$.

compressed gas ahead of it. The semi-periodic structure is prominent in the velocity.

Figure 8 shows the barrel structure at $t = 1.498 \times 10^4 \text{ yr}$. The upper and lower panels denote the density and temperature distributions by color, respectively. The arrows overlaid on the upper panel denote the velocity. As expected, the structure is essentially the same as that illustrated in Figure 2. A hot dense gas flows between the jet boundary and the oblique shock wave. The Mach disk is bent at this stage. See the animation associated with Figure 8 for the formation and evolution of the Mach disk.

Figure 9 shows the longitudinal velocity (v_z) at the stage shown in Figure 7 as a function of z , i.e., the distance from the nozzle. The dark blue curve denotes v_z on the z -axis while the light blue curve shows the maximum of v_z at a given z . The jet flow is not straight as shown in the bottom panel of Figure 7. The longitudinal velocity has a large jump at several places, i.e., at the shock fronts. The Mach number, the ratio of the flow velocity and sound speed, reaches 4.75 and drops suddenly at $z = 293 \text{ au}$, i.e., just in front of the Mach disk. The Mach number exceeds unity at $z = 7.5 \text{ au}$ and the flow is supersonic from there to the Mach disk. The jet flow is off-axis in the range of $300 \text{ au} \lesssim z \lesssim 800 \text{ au}$. The flow is reverse ($v_z < 0$) around the axis in this range. Remember that Figure 4 shows two velocity components

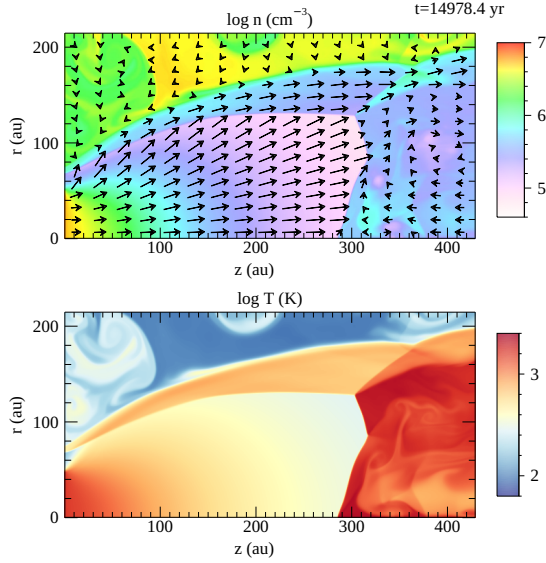


Figure 8. The flow structure in the barrel in model A at $t = 1.498 \times 10^4$ yr. The associated movie shows the fluctuation of the Mach disk. The first barrel is persistent but fluctuates. The animation shows the sequence from zero to 29455.5 years. The duration of the animation is 12 seconds.

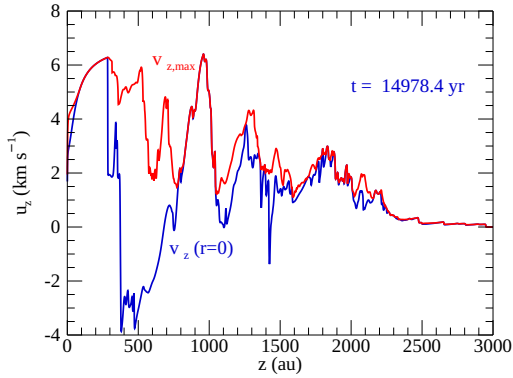


Figure 9. The longitudinal velocity (u_z) at $t = 1.498 \times 10^4$ yr in model A.

along the outflow axis. The blue-shifted may be the off-axis flow along our line of sight while the red-shifted one may be the flow near the outflow axis.

Figures 10 and 11 show the density and temperature distributions on the z -axis at several epochs, respectively. The density and temperature decrease steeply as soon as the gas emerges from the nozzle. Remember that the jet gas has $n_0 = 10^7 \text{ cm}^{-3}$ and $T_0 = 2000 \text{ K}$ at $z = 0$. Also the pressure decreases steeply near the nozzle. Since the pressure ratio is very high $P_0/P_\infty = 40$, the jet gas expands rapidly and adiabatically. The flow

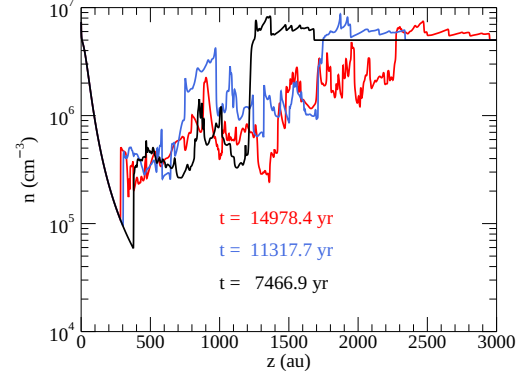


Figure 10. The density distribution on the z -axis in model A at several epochs.

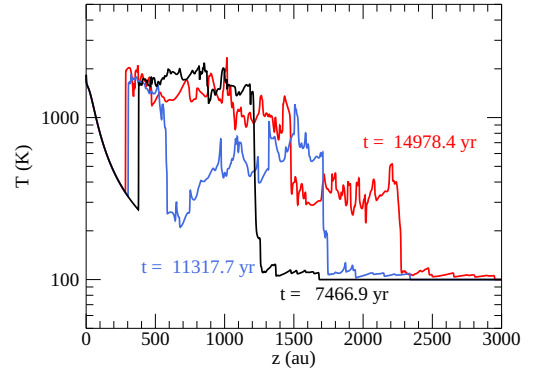


Figure 11. The temperature distribution on the z -axis in model A at several epochs.

is supersonic in the barrel. The density and temperature decrease below 10^5 cm^{-3} and 350 K , respectively, on the upstream side of the Mach disk. They rise again to $5 \times 10^5 \text{ cm}^{-3}$ and $\sim 2000 \text{ K}$ on the downstream side of the Mach disk by the shock compression. This dense hot gas expands again to accelerate the gas ahead. Figures 10 and 11 show the laminar flow in the barrel ($z < 300 \text{ au}$) is stationary while the flow beyond the Mach disk is variable. The head of the jet proceeds at almost constant rate.

We measure the width and height of the barrel from the velocity profile. The tangential and longitudinal components of the velocity (v_r and v_z) are discontinuous on the side of the barrel and at the Mach disk, respectively. We measure the radius where v_r turns to decrease at a given height, z and define it as the local barrel radius. The barrel diameter (D_b) is defined as twice the maximum barrel radius. We define the barrel height as the place where v_z turns to decrease on the

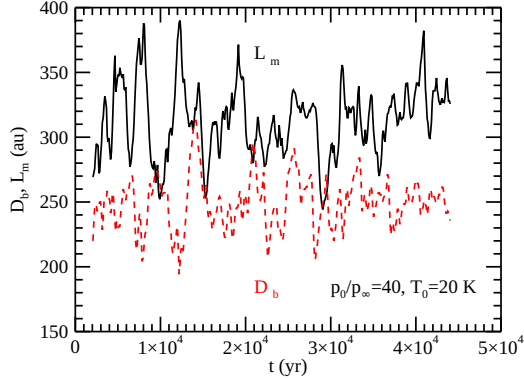


Figure 12. The time evolution of the barrel width (red) and height (black) in model A.

axis ($r = 0$). Figure 12 shows the width and height of the barrel in model A. The height is slightly smaller than expected from Equation (1), 408 au. The height is $\sim 20\%$ larger than the width, though both of them are oscillating substantially. The diameter of the Mach disk is 210 au at the stage shown in Figure 6.

4.3. Higher Pressure Ratio Model

We show model B to examine the effects of a higher pressure ratio. The initial state of model B is the same as that of model A except for the pressure ratio (see Table 1), i.e., the density ratio. The initial density of the injected gas is set to be $n_0 = 10^7 \text{ cm}^{-3}$ for easier comparison with model A. Accordingly, the ambient density is lower in model B. The temperature ratio remains at ($T_0/T_\infty = 20$). Figure 13 is the same as Figure 7 but for the stage at $t = 1.494 \times 10^4 \text{ yr}$ in model B. As shown in the animation associated with Figure 13, models A and B are qualitatively similar.

Figure 14 is the same as Figure 12 but for model B. The first barrel of model B has a larger height and width than that of model A. The aspect ratio, the height over the width is larger in model B, i.e., the first barrel is more slender in model B. Both the height and width of the outflow are larger for a higher pressure ratio. But, the dependence of the width on the pressure ratio is weaker than that of the height. Another difference is the density contrast between the outflow and ambient gas. The ambient gas is less dense in model B.

4.4. Cold Ambient Gas Model

We construct model C in which the ambient gas is set to be cold ($T_\infty = 20 \text{ K}$). The pressure ratio is set to be $P_0/P_\infty = 40$ for comparison with model A. Since the temperature contrast is $T_0/T_\infty = 100$, the ambient gas is 2.5 times denser than that of the injected gas.

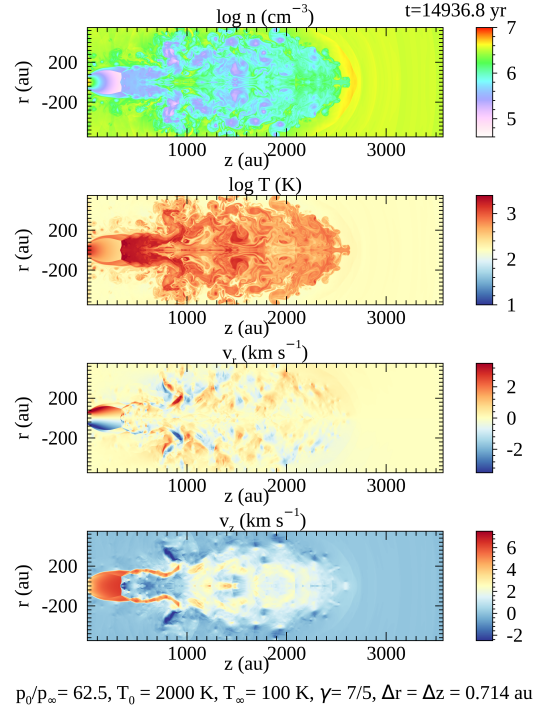


Figure 13. The same as Figure 7 but for model B at $t = 1.494 \times 10^4 \text{ yr}$. The associated animation shows the development of the outflow in model B. The outflow is turbulent and associated with shock waves. The first barrel is persistent. The animation shows the sequence from zero to 20874.4 years. The duration of the animation is 9 seconds.

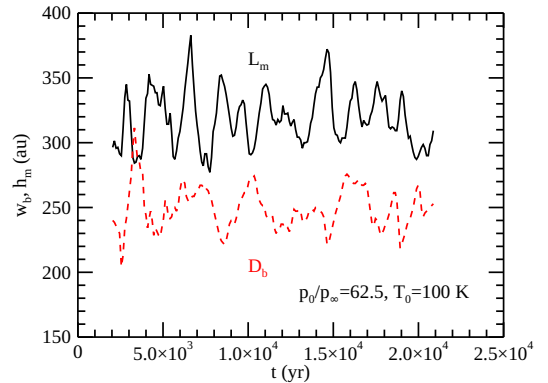


Figure 14. The same as Figure 12 but for model B.

Figure 15 shows the stage at $t = 3.545 \times 10^4 \text{ yr}$ in model C. Model C is also qualitatively similar to models A and B. The outflow shows the barrel and subsequent semi-periodic structure. However, the outflow is less prominent since the ambient gas is much denser. Also the outflow propagates more slowly than in models A and B. The slow propagation is also due to the

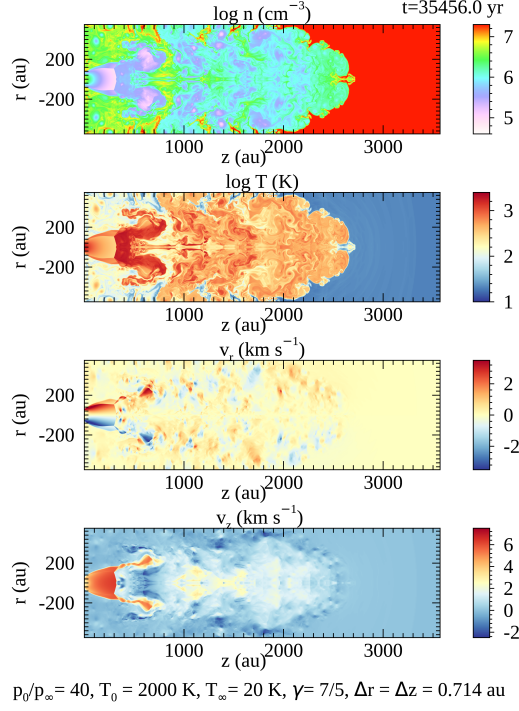


Figure 15. The same as Figure 7 but for model C at $t = 3.545 \times 10^4$ yr. The associated animation shows the development of outflow in model C. The propagation is substantially slower in model C. The animation shows the sequence from zero to 31289.8 years. The duration of the animation is 18 seconds.

dense ambient gas. The larger inertia of the ambient gas decelerates the outflow propagation substantially. This density dependence is similar to that found by [Smith & Keogh \(2022\)](#) though their initial set-up is different.

5. DISCUSSIONS AND SUMMARY

As shown in the previous sections, our simple hydrodynamic model explains several characters of the primary outflow in IRAS 15398–3359. First, it explains the shell structure in the intensity and that in the velocity. Second, it explains the anti-correlation between the temperature and velocity. It also explains the magnitude of the outflow velocity. Equations (3) and (4) suggest that the outflow is accelerated to $\sim 7 \text{ km s}^{-1}$ if most of the initial thermal energy is converted into the kinetic energy at $T_0 = 2000 \text{ K}$. The inferred value is consistent with the observations since the outflow is inclined from our line of sight. Fourth, our model shows a backward ($v_z < 0$) flow in the outflow, which may explain the red-shifted flow in the blue lobe. Our model demonstrates that we need not invoke short time variability in the outflow activity to explain the shell structure.

Our model is an oversimplification in some regards. We assumed that the outflow source maintains constant

pressure, density and temperature after a sudden onset. However, the outflow activity is likely to decay after a short rise. The pressure ratio may be a little higher in the early phase of the primary outflow activity. Uniform density in the source region is also an oversimplification. Thus, we think that our model has limitations to explain the primary outflow of IRAS 15398–3359.

Nevertheless, our model gives some constraints on a better model. First, the ambient gas density should be low enough. The outflow gas is hot ($T > 1000 \text{ K}$) and should have a high pressure to accelerate the gas to be highly supersonic. The density of the outflow gas decreases considerably during the acceleration. If the initial density of the outflow is comparable or lower than that of the ambient gas, the outflow is decelerated by the inertia of the ambient gas (see model C). IRAS 15398–3359 experienced at least two earlier outflow activities ([Okoda et al. 2021a](#); [Sai et al. 2024](#)). The ambient gas around IRAS 15398–3359 can be blown off by the third or even earlier outflow. [Redaelli et al. \(2019\)](#) estimated the gas density to be $n_{\text{H}_2} = 2.6 \times 10^4 \text{ cm}^{-3}$ around IRAS 15398–3359 from the radio and far infrared continuum emission observed with Herschel. They derived the value by approximating the gas cloud to be a uniform sphere having the effective radius 0.1 pc. Thus, this value should be taken as an average in the region of $2 \times 10^4 \text{ au}$ around IRAS 15398–3359. If the gas density around the primary outflow is similarly low, the outflowing gas will have a higher density than the ambient gas if the outflowing gas has the initial density $n_{\text{H}_2} \approx 10^7 \text{ cm}^{-3}$. Second, the gas temperature should be as high as 2000 K around the protostar. The outflow gas has a high temperature ($T > 1000 \text{ K}$, [Okoda et al. 2025](#)) and substantial velocity. This implies the outflow gas has a higher temperature before acceleration unless it is heated up during the acceleration. Third, the source of the outflow should have a radial size of $\sim 50 \text{ au}$ if the first shell located at 300 au from the protostar is due to the Mach disk.

Though JWST observed IRAS 15398–3359, the measurement of the gas temperature is limited to a narrow region around the protostar (see Figure 8 of [Okoda et al. 2025](#)), i.e., the field of view of the spectroscopic observation. It is interesting to measure the temperature and density in the outflow beyond the second shell. Similarly, ALMA observed only a limited portion of the primary outflow with the highest observation ([Thieme et al. 2023](#)). It would be interesting to study the kinematics around shells 3 and 4 with ALMA.

Also interesting is to study outflows showing similar substructures. Herbig-Haro 211 (hereafter HH 211) is an example showing a similar substructure in the CO

($J = 2-1$) (Gueth & Guilloteau 1999)) and H_2 ($2.1\ \mu\text{m}$) (McCaughrean et al. 1994) emission lines. Figure 1 of Cabrit et al. (2011) shows the correlation between the substructures. The infrared emission from HH 211 was further studied with Spitzer telescope Tappe et al. (2012) and JWST (Ray et al. 2023). Ray et al. (2023) identified that the $4.5\ \mu\text{m}$ localized emissions are largely due to the CO fundamental rotational-vibrational transitions. This means that the CO gas is hot ($\sim 1000\ \text{K}$) only in the narrow regions where the $4.5\ \mu\text{m}$ emission is strong. Other examples are CALMA 7 and DG Tau B. Plunkett et al. (2015) discovered semi-regularly placed knots in the outflow from CARMA 7, a Class 0 source in the Serpens South star forming region. They found 11 knots each in the red and blue lobes. (de Valon et al. 2020) discovered shell structure in the outflow cavity of DG Tau B. The shells appear near the protostar in the widely open conical cavity. We may find other examples from archival data of ALMA.

ACKNOWLEDGEMENTS

This work is supported by the MEXT/JSPS Grant-in-Aid from the Ministry of Education, Culture, Sports, Science, and Technology of Japan (20H00182, 20H05844, 20H05845, 20H05847, and 22K20389). Y.O., Y.-L.Y., and N.S. are grateful for support from the RIKEN pioneering project: Evolution of Matter in the Universe. Y. O. is supported by RIKEN Special Postdoctoral Re-

searcher Program (Fellowships) and the Japan Society for the Promotion of Science (JSPS), Overseas Research Fellowship. Japan Society for the Promotion of Science (JSPS), Overseas Research Fellowship. This work is based in part on observations made with the NASA/ESA/CSA James Webb Space Telescope. The data were obtained from the Mikulski Archive for Space Telescopes at the Space Telescope Science Institute, which is operated by the Association of Universities for Research in Astronomy, Inc., under NASA contract NAS 5-03127 for JWST. These observations are associated with program #2151. The data were retrieved from the Mikulski Archive for Space Telescopes at the Space Telescope Science Institute, operated by the Association of Universities for Research in Astronomy (AURA), Inc., under NASA contract NAS 5-03127. The data presented in this paper were obtained from the Mikulski Archive for Space Telescopes (MAST) at the Space Telescope Science Institute. The specific observations analyzed can be accessed via DOI: [10.17909/wv1n-rf97](https://doi.org/10.17909/wv1n-rf97) and Salyk et al. (2024). This paper makes use of the following ALMA data: ADS/JAO.ALMA#2013.1.00879.S and ADS/JAO.ALMA#2018.1.01205.L. ALMA is a partnership of the ESO (representing its member states), the NSF (USA) and NINS (Japan), together with the NRC (Canada) and the NSC and ASIAA (Taiwan), in cooperation with the Republic of Chile. The Joint ALMA Observatory is operated by the ESO, the AUI/NRAO, and the NAOJ.

REFERENCES

- Addy, A. L. 1981, *AIAA Journal*, 19, 121, doi: [10.2514/3.7751](https://doi.org/10.2514/3.7751)
- Bushouse, H., Eisenhamer, J., Dencheva, N., et al. 2023, *JWST Calibration Pipeline*, 1.12.5, Zenodo, doi: [10.5281/zenodo.10022973](https://doi.org/10.5281/zenodo.10022973)
- . 2024, *JWST Calibration Pipeline*, 1.14.0, Zenodo, doi: [10.5281/zenodo.10870758](https://doi.org/10.5281/zenodo.10870758)
- Cabrit, S., Ferreira, J., & Dougados, C. 2011, in *IAU Symposium*, Vol. 275, *Jets at All Scales*, ed. G. E. Romero, R. A. Sunyaev, & T. Belloni, 374–382, doi: [10.1017/S1743921310016431](https://doi.org/10.1017/S1743921310016431)
- Codella, C., Ceccarelli, C., Chandler, C., et al. 2021, *Frontiers in Astronomy and Space Sciences*, 8, 227, doi: [10.3389/fspas.2021.782006](https://doi.org/10.3389/fspas.2021.782006)
- Crist, S., Glass, D. R., & Sherman, P. M. 1966, *AIAA Journal*, 4, 68, doi: [10.2514/3.3386](https://doi.org/10.2514/3.3386)
- de Valon, A., Dougados, C., Cabrit, S., et al. 2020, *A&A*, 634, L12, doi: [10.1051/0004-6361/201936950](https://doi.org/10.1051/0004-6361/201936950)
- Franquet, E., Perrier, V., Gibout, S., & Bruel, P. 2015, *Progress in Aerospace Sciences*, 77, 25, doi: [10.1016/j.paerosci.2015.06.006](https://doi.org/10.1016/j.paerosci.2015.06.006)
- Galli, P. A. B., Bouy, H., Olivares, J., et al. 2020, *A&A*, 643, A148, doi: [10.1051/0004-6361/202038717](https://doi.org/10.1051/0004-6361/202038717)
- Gueth, F., & Guilloteau, S. 1999, *A&A*, 343, 571
- Guzmán Ccolque, E., Fernández López, M., Vazzano, M. M., et al. 2024, *A&A*, 686, A143, doi: [10.1051/0004-6361/202348816](https://doi.org/10.1051/0004-6361/202348816)
- Hanawa, T., Garufi, A., Podio, L., Codella, C., & Segura-Cox, D. 2024, *MNRAS*, 528, 6581, doi: [10.1093/mnras/stae338](https://doi.org/10.1093/mnras/stae338)
- Hanawa, T., & Matsumoto, Y. 2021, *ApJ*, 907, 43, doi: [10.3847/1538-4357/abd2b2](https://doi.org/10.3847/1538-4357/abd2b2)
- Hanawa, T., Sakai, N., & Yamamoto, S. 2022, *ApJ*, 932, 122, doi: [10.3847/1538-4357/ac6e6a](https://doi.org/10.3847/1538-4357/ac6e6a)
- Hatanaka, K., & Saito, T. 2012, *Shock Waves*, 22, 427, doi: [10.1007/s00193-012-0391-x](https://doi.org/10.1007/s00193-012-0391-x)

- Komissarov, S. S., & Falle, S. A. E. G. 1998, *MNRAS*, 297, 1087, doi: [10.1046/j.1365-8711.1998.01547.x](https://doi.org/10.1046/j.1365-8711.1998.01547.x)
- Matsushita, Y., Takahashi, S., Ishii, S., et al. 2021, *ApJ*, 916, 23, doi: [10.3847/1538-4357/ac069f](https://doi.org/10.3847/1538-4357/ac069f)
- McCaughrean, M. J., Rayner, J. T., & Zinnecker, H. 1994, *ApJL*, 436, L189, doi: [10.1086/187664](https://doi.org/10.1086/187664)
- Norman, M. L., Winkler, K. H. A., Smarr, L., & Smith, M. D. 1982, *A&A*, 113, 285
- Okoda, Y., Oya, Y., Francis, L., et al. 2021a, *ApJ*, 910, 11, doi: [10.3847/1538-4357/abddb1](https://doi.org/10.3847/1538-4357/abddb1)
- . 2021b, *ApJ*, 910, 11, doi: [10.3847/1538-4357/abddb1](https://doi.org/10.3847/1538-4357/abddb1)
- . 2023, *ApJ*, 948, 127, doi: [10.3847/1538-4357/acc1e5](https://doi.org/10.3847/1538-4357/acc1e5)
- Okoda, Y., Yang, Y.-L., Evans, II, N. J., et al. 2025, *ApJ*, 982, 149, doi: [10.3847/1538-4357/ad83f](https://doi.org/10.3847/1538-4357/ad83f)
- Oya, Y., Sakai, N., Sakai, T., et al. 2014, *ApJ*, 795, 152, doi: [10.1088/0004-637X/795/2/152](https://doi.org/10.1088/0004-637X/795/2/152)
- Plunkett, A. L., Arce, H. G., Mardones, D., et al. 2015, *Nature*, 527, 70, doi: [10.1038/nature15702](https://doi.org/10.1038/nature15702)
- Ray, T. P., McCaughrean, M. J., Caratti o Garatti, A., et al. 2023, *Nature*, 622, 48, doi: [10.1038/s41586-023-06551-1](https://doi.org/10.1038/s41586-023-06551-1)
- Redaelli, E., Alves, F. O., Santos, F. P., & Caselli, P. 2019, *A&A*, 631, A154, doi: [10.1051/0004-6361/201936271](https://doi.org/10.1051/0004-6361/201936271)
- Sai, J., Yen, H.-W., Machida, M. N., et al. 2024, *ApJ*, 966, 192, doi: [10.3847/1538-4357/ad34b7](https://doi.org/10.3847/1538-4357/ad34b7)
- Salyk, C., Yang, Y.-L., Pontoppidan, K. M., et al. 2024, *ApJ*, 974, 97, doi: [10.3847/1538-4357/ad62fe](https://doi.org/10.3847/1538-4357/ad62fe)
- Shang, H., Liu, C.-F., Krasnopolsky, R., & Wang, L.-Y. 2023, *ApJ*, 944, 230, doi: [10.3847/1538-4357/aca763](https://doi.org/10.3847/1538-4357/aca763)
- Smith, M. D., & Keogh, T. L. R. 2022, *MNRAS*, 516, 2757, doi: [10.1093/mnras/stac2310](https://doi.org/10.1093/mnras/stac2310)
- Smith, M. D., & Richards, C. 2023, *MNRAS*, 526, 3407, doi: [10.1093/mnras/stad2879](https://doi.org/10.1093/mnras/stad2879)
- Tachihara, K., Dobashi, K., Mizuno, A., Ogawa, H., & Fukui, Y. 1996, *PASJ*, 48, 489, doi: [10.1093/pasj/48.3.489](https://doi.org/10.1093/pasj/48.3.489)
- Tappe, A., Forbrich, J., Martín, S., Yuan, Y., & Lada, C. J. 2012, *ApJ*, 751, 9, doi: [10.1088/0004-637X/751/1/9](https://doi.org/10.1088/0004-637X/751/1/9)
- Thieme, T. J., Lai, S.-P., Ohashi, N., et al. 2023, *ApJ*, 958, 60, doi: [10.3847/1538-4357/ad003a](https://doi.org/10.3847/1538-4357/ad003a)
- Vazzano, M. M., Fernández-López, M., Plunkett, A., et al. 2021, *A&A*, 648, A41, doi: [10.1051/0004-6361/202039228](https://doi.org/10.1051/0004-6361/202039228)
- Yang, Y.-L., Green, J. D., Pontoppidan, K. M., et al. 2022, *ApJL*, 941, L13, doi: [10.3847/2041-8213/aca289](https://doi.org/10.3847/2041-8213/aca289)
- Yen, H.-W., Koch, P. M., Takakuwa, S., et al. 2017, *ApJ*, 834, 178, doi: [10.3847/1538-4357/834/2/178](https://doi.org/10.3847/1538-4357/834/2/178)
- Yen, H.-W., Takakuwa, S., Ohashi, N., & Ho, P. T. P. 2013, *ApJ*, 772, 22, doi: [10.1088/0004-637X/772/1/22](https://doi.org/10.1088/0004-637X/772/1/22)
- Young, W. S. 1975, *Physics of Fluids*, 18, 1421, doi: [10.1063/1.861039](https://doi.org/10.1063/1.861039)
- Yu, J., Vuorinen, V., Kaario, O., Sarjovaara, T., & Larmi, M. 2013, *International Journal of Heat and Fluid Flow*, 44, 140, doi: [10.1016/j.ijheatfluidflow.2013.05.015](https://doi.org/10.1016/j.ijheatfluidflow.2013.05.015)